

New data processing of local heat transfer coefficient inside a rectangular channel

P Gramazio, L Vitali, D Fustinoni, and A Niro

Politecnico di Milano, Department of Energy,
Campus Bovisa, Via Lambruschini 4, 20156 Milano, Italy

E-mail: alfonso.niro@polimi.it

Abstract. In this paper, we critically reconsider and discuss the models used in one of our previous work to calculate the local convective heat flux for forced air-flows inside narrow rectangular channel, in order to evaluate the limitations which may be inherent with them. To this end, several numerical FEM models have been developed in COMSOL™ and used to analyze in depth previous data processing procedures; furthermore, experimental tests are made on the channel materials, to determine their thermal conductivities and radiative properties. Here, the results of this analysis are presented and discussed.

1 Introduction

Forced air-flows inside narrow rectangular channels are frequently encountered in many “compact” heat transfer devices. Because of small passages and relatively low air velocity, however, heat transfer is rather poor, and hence a number of specially configured extended-surfaces are used to overcome this limit. Ribs are an efficient and cost-effective way to enhance heat transfer without overmuch penalizing pressure drops. For this reason, a long-term experimental campaign has been carried out at the ThermALab of Energy Department of Politecnico di Milano on heat transfer characteristics in forced convection through rectangular channels with one or two rib-roughened surfaces in a very large variety of configurations.

The present work originates from our previous endeavors in measuring the local convective heat transfer coefficient in transitioning flow regimes inside a channel with only the bottom surface heated and ribbed [1]. Indeed, their spanwise-averaged values, for both ribbed and flat reference configurations, were in good agreement with the corresponding average results directly measured in previous works [2] and, for the flat reference channel, validated with the literature results [3]. However, the local heat transfer coefficient, as shown in figure 1, displayed an unexpected increasing trend while approaching the channel side walls. Although it could drop to zero within a thickness too small to be seen, we conjecture it to be an effect of the adopted processing technique. More precisely, to derive the convective heat flux from the heating rate measurement, we have to take into account and evaluate all the other contributions to heat transfer. Thus, accurate conductive and radiative models are needed to retrieve the information on heat fluxes from local temperature measurements; on other hand, the thermophysical properties of materials should be known with the greater possible accuracy.

In this paper, a critical assessment of the models already used to calculate the local convective heat flux has been carried out, in order to evaluate the limitations which may be inherent with them. Furthermore, experimental tests are made on the channel materials, to determine their thermal

conductivities and radiative properties. The final objective is to understand and assess how each calculated heat flux affects the evaluation of the local heat transfer coefficient, and to improve the models to reduce the estimated error. To this end, several models have been developed in COMSOL™ FEM and are used as tools to better understand the limitations of the previously utilized models.

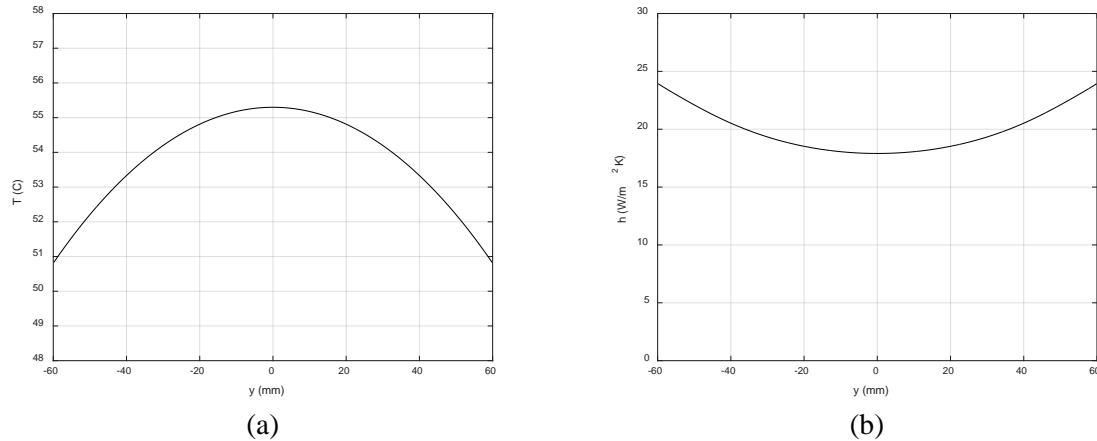


Figure 1. Temperature distribution (a) and local heat transfer coefficient (b), $Re = 5400$, presented in [1], non-ribbed bottom surface.

2 Materials and methods

2.1 Open-loop wind channel

The experimental setup has been thoroughly presented in [1]; here, just a brief description is reported in order to better focus the problem. It consists of an insulated open-loop wind tunnel operated in suction, schematically shown in figure 2, with a 120 mm wide, 12 mm high test section, whose main features are summarized in table 1. The channel is heated with two independently powered and controlled printed circuit boards (PCB), and the air flow is regulated by means of a valve system. A Hendress Hauser T-Mass 65F15 flow meter is used for automatic mass-flow readings. A double-glazing 130 mm x 130 mm germanium window grants the optical access to a FLIR T650sc IR-camera, which measures the temperature field of the breadboard surface due to the calibration procedure also described in [1]. The channel is also equipped with 10 temperature sensors, 4 RTDs and 6 thermocouples, to measure the average temperatures of the inlet and outlet flow, of the internal germanium window, and of the channel wall beneath the heater.

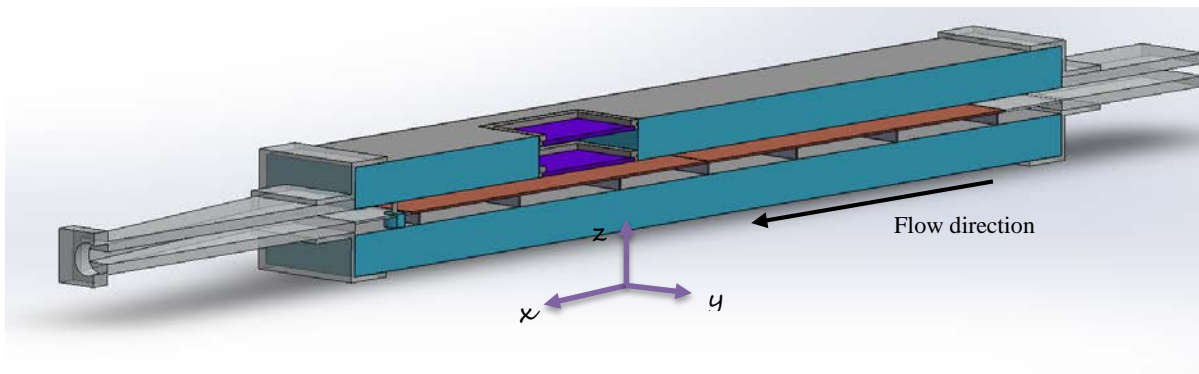


Figure 2. Open-loop wind tunnel design, vertical cross-section

Table 1. main experimental features

H	Channel height	12 mm
L	Channel length	840 mm
w	Channel width	120 mm
D_h	Hydraulic diameter	21.82 mm
H/w	Height to width ratio	0.10
s	Rib side dimension	4 mm
d	Distance rib-to-rib	80 mm
Re	Reynolds number	700 ÷ 8000

2.2 Radiative properties measurements

For an opaque surface, the hemispherical spectral emissivity ε_λ equals the hemispherical spectral absorptance α_λ which in turn, for diffuse radiation, is the complement to 1 of the hemispherical spectral reflectance ρ_λ . On other hand, in term of directional-hemispherical spectral reflectance $\rho'_\lambda(\lambda, \theta_i)$, i.e., the energy reflected into all directions due to intensity incoming from a single direction, the hemispherical spectral reflectance ρ_λ is

$$\rho_\lambda(\lambda) = \frac{\int_{2\pi} \rho'_\lambda(\lambda, \vartheta_i) I_\lambda(\lambda, \vartheta_i) \cos \vartheta_i d\Omega_i}{\int_{2\pi} I_\lambda(\lambda, \vartheta_i) \cos \vartheta_i d\Omega_i} \quad (1)$$

If the incident intensity is independent of direction (diffuse radiation), the previous equation becomes

$$\rho_\lambda(\lambda) = \frac{1}{\pi} \int_{2\pi [sr]} \rho'_\lambda(\lambda, \vartheta_i) \cos \vartheta_i d\Omega_i = 2 \int_0^{\pi/2 [rad]} \rho'_\lambda(\lambda, \vartheta_i) \cos \vartheta_i \sin \vartheta_i d\vartheta_i \quad (2)$$

For optically smooth non-conductors and for unpolarized radiation incident from a gas, the directional-hemispherical spectral reflectance $\rho'_\lambda(\lambda, \theta_i)$ can be evaluated by the following expression derived from the electromagnetic wave theory [4]

$$\rho'_\lambda(\lambda, \vartheta_i) = \frac{1}{2} \left[\left(\frac{n^2 \cos \vartheta_i - \sqrt{n^2 - \sin^2 \vartheta_i}}{n^2 \cos \vartheta_i + \sqrt{n^2 - \sin^2 \vartheta_i}} \right)^2 + \left(\frac{\cos \vartheta_i - \sqrt{n^2 - \sin^2 \vartheta_i}}{\cos \vartheta_i + \sqrt{n^2 - \sin^2 \vartheta_i}} \right)^2 \right] \quad (3)$$

where n the refractive index of the medium. By means of the Perkin Elmer Frontier FT-IR spectrophotometer equipped with a 3-inch integrating gold sphere, $\rho'_\lambda(\lambda, \theta_i)$ has been measured in the Mid-IR range and for a near normal incidence direction, i.e., $\theta_i = 12^\circ$, for the three main kinds of surfaces enclosing the test-section sensed portion, namely, panels in extruded polystyrene foam (XPS), parts in acrylic glass (PMMA), and the printed circuit board (PCB). Figure 3 displays these values plotted vs wavelength. By solving equation 3 with respect n for $\theta_i = 12^\circ$ and using the measured value of $\rho'_\lambda(\lambda, \theta_i)$ of each surface, the corresponding refractive index has been evaluated. Finally, by substituting equation 3 into equation 2 and then numerically integrating, the values of ρ_λ and hence ε_λ were found.

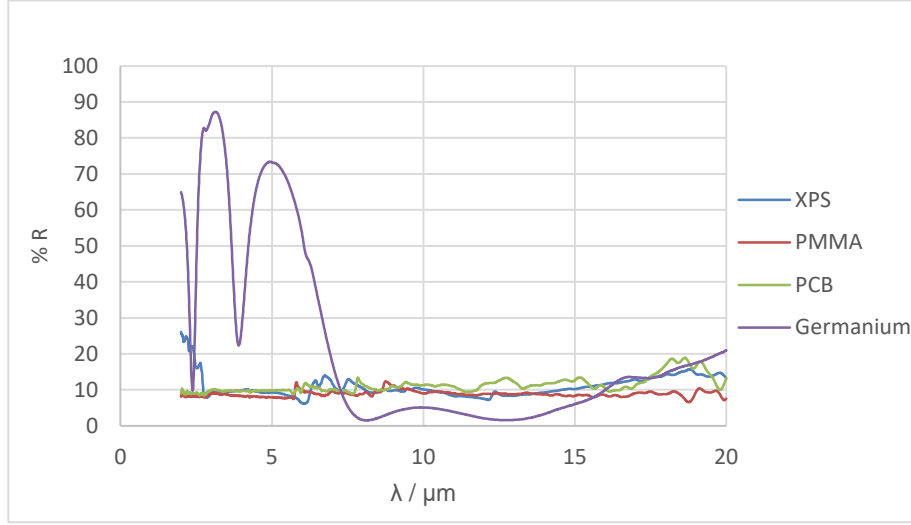


Figure 3. Directional-hemispherical spectral reflectance, Mid-IR wavelength range

2.3 Thermal conductivity measurements

Thermal conductivity for the same three materials, i.e., XPS, PCB and PMMA, has been measured by means of the C-Therm TCi™ instrument by C-Therm Technologies, whose accuracy and precision are better than 5% and 1%, respectively, as tested with reference materials. Table 2 lists the measured values of thermal conductivity.

Table 2. Thermal conductivities of the three main materials in the test-section

Material	Conductivity [W/mK]
XPS	0.02
PMMA	0.30
PCB	0.30

3 Modeling of the experiment

3.1 Local convective heat flux evaluation

By a steady-state energy balance for a unit-volume of the heater of infinitesimal base area $dx \cdot dy$ and height $s = (s_{cu} + s_{pcb})$, i.e., equal to the sum of copper track and breadboard thicknesses, we obtain

$$q_c(x, y) = q_{el} - q_r(x, y) - q_{kz}(x, y) + \int_{z=0}^{z=s_{cu}+s_{pcb}} k(z) \left(\frac{\partial^2 T(x, y, z)}{\partial x^2} + \frac{\partial^2 T(x, y, z)}{\partial y^2} \right) dz \quad (4)$$

where q_{el} the heat generated by Joule effect in the PCB copper tracks, which is supposed to be uniform, $q_r(x, y)$ the heat loss by radiation from the PCB upward surface, and $q_{kz}(x, y)$ the heat loss from the PCB backside. The last term in equation 4 is the divergence of the conductive heat flux through the PCB plane integrated along its thickness which, for the sake of brevity, we refer to as the pseudo-conductive heat flux q_{kxy} . Each term needs a dedicated model in order to be evaluated from the experimental measurements. In the following subsections, we focus on the discussion of these models. Once all these terms are evaluated, the local convective heat transfer coefficient can be retrieved as

$$h(x, y) = \frac{q_c(x, y)}{T_w(x, y) - T_b(x)} \quad (5)$$

The experiments reported in our previous work produced the estimate of the average relative contribution of the heat flux terms to the overall energy balance, as shown in figure 4. The radiative heat flux could seemingly be the most relevant term, whereas the pseudo-conductive heat flux and backside one should lose importance with increasing Reynolds numbers. However, it is noteworthy to keep in mind that local relative contribution can be significantly different from the average one, especially in proximity of the side walls.

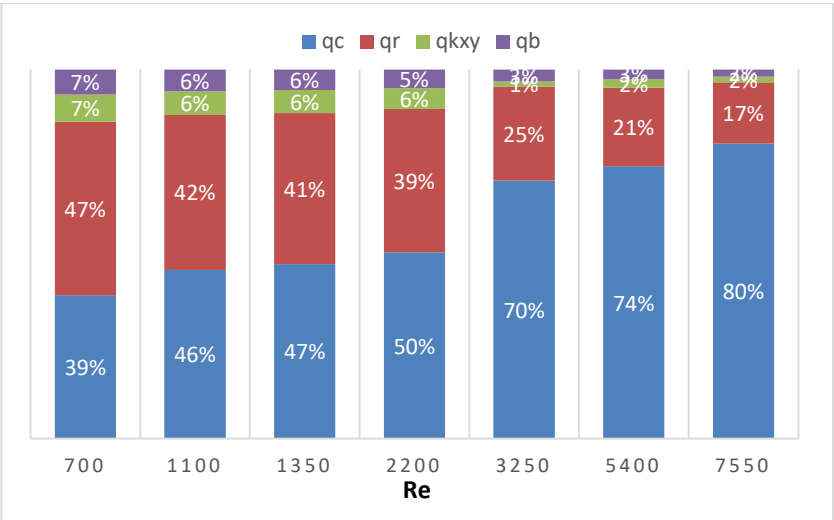


Figure 4. Relative heat flux distribution, as a function of Reynolds number

3.2 Numerical FEM model of the section

A detailed 2D numerical FEM heat transfer model of a y-z transverse section of the test-section has been developed in COMSOL™, featuring all its components as shown in figure 5, namely, PCB, PMMA frames, germanium double window, insulating walls, and the layer of still air underlying the PCB. The convective heat transfer coefficient and the bulk flow temperature are imposed as boundary conditions in the only non-modelled region, i.e., the internal channel where air flows through. Finally, the radiative heat exchange between the channel inside walls is solved too by COMSOL™ but with a model for opaque surfaces. Convective and radiative heat transfer from the test-section outside walls to laboratory environment is imposed on them as boundary conditions. The simulations yield the temperature field in the computational domain, and are used as benchmark to test the heat flux modes.

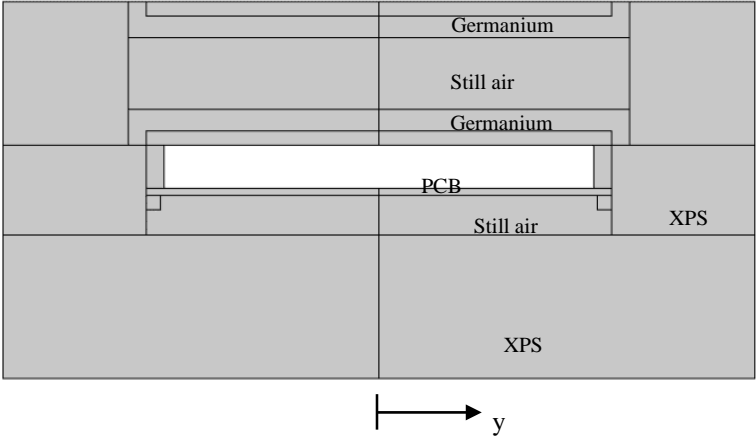


Figure 5. Geometry of the COMSOL™ FEM model of the complete test section

3.3 Electric heat flux

The electric heater is made of thin copper tracks that lay on the board substrate; they cover 97.5% of the surface exposed to the air flow. In our calculation, a spatially uniform generated heat flux is assumed. The correctness of this assumption has been specifically verified by measuring the heater surface temperature by means of IR thermography while being operated in open air and, hence, subject only to natural convection. The acquired temperature field has been compared with the results of a CFD non stationary model of natural convection for the same geometry, with uniform heat generation. The local temperature difference between model and experiment was less than 5%, therefore proving the hypothesis to be adequate, to our best knowledge.

3.4 Radiative heat flux

A radiative heat transfer model is needed to precisely evaluate the local radiative heat flux $q_r(x,y)$, from the thermographic measurement of the local temperature on the PCB surface and the temperature measurements by means of thermocouples on the germanium window. To this end, a first Matlab® model was developed in [1], for the ease of interfacing it with the acquired thermograms, based on Modest's model [4] for opaque, gray and diffuse enclosures, with an added term that takes into account the estimated radiative losses, due to the partial IR-transparency of the germanium windows. The model solves the radiative heat transfer problem in a 2D cavity, which is a y - z slice of the test section, by discretizing the bottom surface, i.e. the heater, with N_y elements, while the remaining three surfaces were modelled with one element each, as their temperature was supposed to be position-independent. The view factors were calculated by means of the Hottel's method. This model showed some deviation from the expected results, especially near the edges, when tested with low emissivity top surfaces.

This model has been improved, using a radiative COMSOL™ model as benchmark to evaluate the accuracy in specific test cases for opaque surfaces. The equation set is now based on a slight modified version of the Siegel's model [5], which describes the radiative heat transfer for cavities composed by semi-transparent, diffuse and selective surfaces, as shown in equations 6 – 10. In addition, all surfaces are now discretized, with the same number of elements for opposite surfaces, i.e. N_y for the top and bottom surfaces, and N_z for each side, being N_y the pixel number in y -direction of a thermogram, equal to 433. Furthermore, the spectral behaviour was introduced, by considering three wavelength regions with constant optical properties, i.e., between 0 and 7 μm , 7 and 13 μm , and from 13 μm up.

Moreover, whereas the top temperature is considered to be constant because of the high conductivity of the Germanium window, several numerical tests have also been carried out to evaluate the best estimate of the side walls temperature $T_s(z)$, which is not experimentally determined, on the basis of the top and bottom-side measurements. The linear approximation showed a good agreement in the resulting heat flux trend, while a constant approximation showed a better matching in a broad central region; so the latter was eventually adopted.

Finally, the better geometrical discretization led to an improvement of the accuracy of the view factors, especially near the edges, influencing the trend of the radiative heat flux, while the experimental measurement of the radiative properties affected its estimated value, which now results 20% larger than that previously modelled, as it can be seen in figure 6.

$$\begin{aligned}
 & \sum_{j=1}^N \frac{1}{E_{w,j}^{(k)}} \left(\delta_{kj} - R_{w,j}^{(k)} F_{kj} \right) \left[q_j^{(k)} - E_{w,j}^{(k)} \sigma T_j^4 F_{0\lambda}^{(k)} \right. \\
 & \quad \left. + \left(1 - R_{w,j}^{(k)} \right) q_{e,j}^{(k)} \right] \\
 & = \sum_{j=1}^N \left(\sigma T_j^4 F_{0\lambda}^{(k)} + \frac{T_{w,j}^{(k)}}{E_{w,j}^{(k)}} q_{e,j}^{(k)} \right) \left[\delta_{kj} \right. \\
 & \quad \left. - \left(1 - T_{w,j}^{(k)} \right) F_{kj} \right]
 \end{aligned} \tag{6}$$

$1 \leq j \leq N$
 $k: \lambda_1 \leq \lambda \leq \lambda_2$

$$q_j = \sum_{k=1}^{N_\lambda} q_j^{(k)} \quad (7)$$

$$R_{w,j}^{(k)} = \rho^{(k)} \left[1 + \frac{(1 - \rho^{(k)})^2 \tau^{(k)2}}{1 - \rho^{(k)2} \tau^{(k)2}} \right] \quad (8)$$

$$T_{w,j}^{(k)} = \tau^{(k)} \frac{1 - \rho^{(k)}}{1 + \rho^{(k)}} \frac{1 - \rho^{(k)2}}{1 - \rho^{(k)2} \tau^{(k)2}} \quad (9)$$

$$E_{w,j}^{(k)} = A_{w,j}^{(k)} = \frac{(1 - \rho^{(k)})(1 - \tau^{(k)})}{1 - \rho^{(k)} \tau^{(k)}} \quad (10)$$

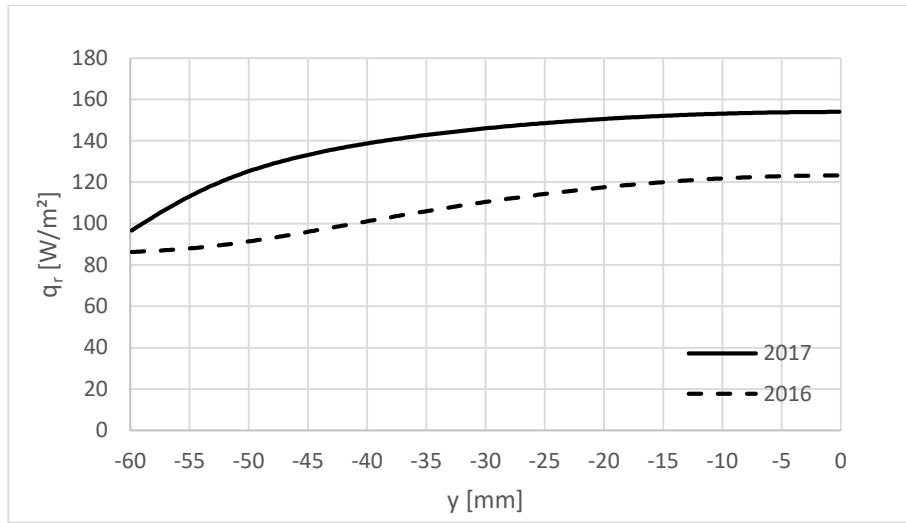


Figure 6. Radiative heat flux, comparison between ref. [1] (2016) and present work (2017).

3.5 Breadboard conductive heat flux

In our previous work, the pseudo-conductive heat flux q_{kxy} in the breadboard plane was calculated with equation 11, under the hypothesis of the uniformity of the surface temperature over the copper tracks thickness. The model can be extended by using a combined copper and PCB conductivity, as shown in equation 12, yet considering temperature to be uniform over the entire PCB thickness. The effectiveness of the latter assumption, has been tested by using the numerical FEM model presented in subsection 3.2, which allowed to compare the span-wise distribution of the pseudo-conductive heat flux evaluated with equation 12, i.e., using only the surface-temperature field numerically obtained, with that evaluated by means of equation 13 taking advantage of fully knowing the y - z temperature field inside the PCB.

$$q_{kxy.1}(x, y) = k_{Cu} s_{Cu} \left(\frac{\partial^2 T_w(x, y)}{\partial x^2} + \frac{\partial^2 T_w(x, y)}{\partial y^2} \right) \quad (11)$$

$$q_{kxy.2}(x, y) = (k_{Cu} s_{Cu} + k_{PCB} s_{PCB}) \left(\frac{\partial^2 T_w(x, y)}{\partial x^2} + \frac{\partial^2 T_w(x, y)}{\partial y^2} \right) \quad (12)$$

$$q_{kxy}(x, y) = k_{Cu} \int_0^{z_{Cu}} \left(\frac{\partial^2 T(x, y, z)}{\partial x^2} + \frac{\partial^2 T(x, y, z)}{\partial y^2} \right) dz + k_{PCB} \int_0^{z_{PCB}} \left(\frac{\partial^2 T(x, y, z)}{\partial x^2} + \frac{\partial^2 T(x, y, z)}{\partial y^2} \right) dz \quad (13)$$

The results are compared in figure 7, which highlights that the two pseudo-conductive heat flux distributions differ each other by a mere 1% in the central region, i.e., for y ranging from -50 to 50 mm, but they are completely different, even changing their concavity, while moving toward the edges. Since experimentally it is possible only measuring the surface-temperature distribution, we are obliged to evaluate q_{kxy} by means of equation 12, but we have to keep well in mind however that it adequately predicts the pseudo-conductive heat flux in a quite wide region but not in nearness of the side walls where error becomes huge.

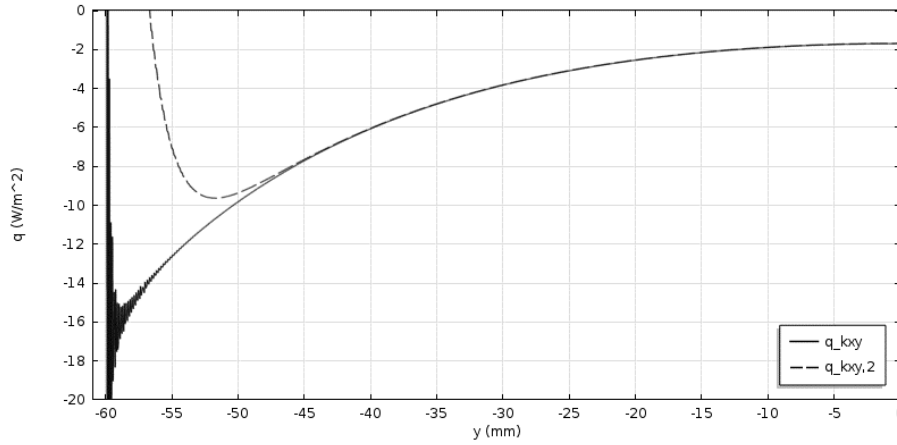


Figure 7. Pseudo-conductive heat flux, numerical results, model based on surface temperature and average over the thickness, $Re = 5400$.

3.6 Backside conductive heat flux

The heat flux dispersed from the PCB backside was evaluated under the assumption of using a simple 1D conductive model, as shown in equation 14, applied on each thermogram pixel

$$q_{kz.1}(x, y) = \frac{k_{air}}{s_{air}} [T_w(x, y) - T_{int}] \quad (14)$$

where $T_w(x, y)$ the PCB upper surface temperature, and T_{int} the temperature on the bottom side of the air layer. It can be seen that only the still air insulating layer was taken into account, and that an average internal temperature was used for the calculation. This model can be improved by considering the conductive resistance of the PCB in addition to that of air layer (equation 15), but further considerations are needed because of the results of the numerical FEM model shown in figure 8. Indeed, the spanwise trend of q_{kz} numerically evaluated shows a very different behavior with respect to that of the 1D model.

$$q_{kz.2}(x, y) = \left(\frac{k_{air}}{s_{air}} + \frac{k_{PCB}}{s_{PCB}} \right) [T_w(x, y) - T_{int}] \quad (15)$$

The adopted solution is therefore to use instead of the local temperature $T_w(x,y)$ its spanwise-averaged value $T_{w.av}(x)$, which yields our best estimate as it reduces the error by about 50% in the most part of the spanwise y-direction

$$q_{kz.3}(x,y) = \frac{k_{air}}{S_{air}} [T_{w.av}(x) - T_{int}] \quad (16)$$

The accuracy of the q_{kz} estimate can be improved only by considering a more complex numerical 2D model, which by now is beyond the scope of this work but that may be integrated in the future. A summary of the main improvements and modifications is reported in table 3.

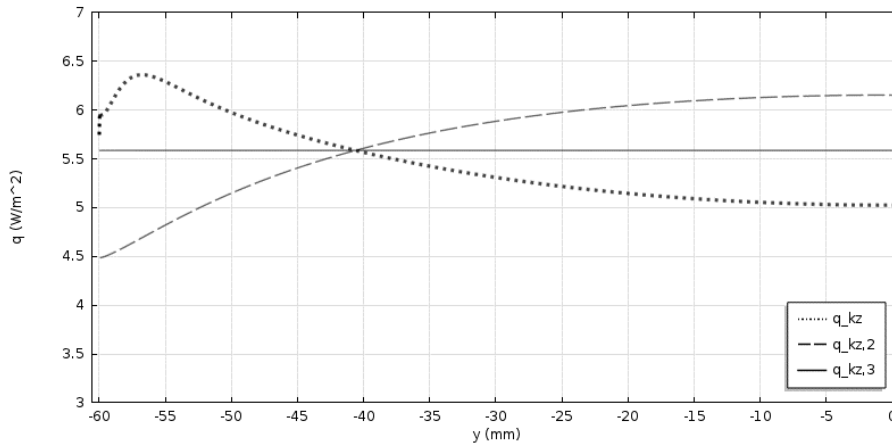


Figure 8. Comparison between three ways of calculating the backside conductive heat flux, and the numerical trend, $Re = 5400$.

Table 3. Model comparison

Model	Previous version	New version
Radiative (q_r)	Modest's model	Modified Siegel's model
	One element top and sides	N_y elements top/bottom, N_z elements each side
	No spectral behavior	Constant properties in N_λ custom bands
	Linear T_s	Constant T_s
Conductive (q_{kxy})	Copper-only conductivity	Combined copper-PCB conductivity $q_{kxy.2}$
Conductive back	1D, $q_{kz.1}$	1D $q_{kz.3}$

4 Results

4.1 Experimental local convective coefficient

By using the experimental data for the flat channel reported in [1], and calculating the convective heat flux as

$$q_c'(x,y) = q_{el} - q_r(x,y) + q_{kxy.2}(x,y) - q_{kz.3}(x,y) \quad (17)$$

equation 5 yields the local heat transfer coefficient h' , where the prime for both q_c and h remarks they are approximations. In figure 9, h' is plotted versus the y direction. As it can be seen, the new processing procedure reduces slightly, and almost uniformly, the value of h' mainly because of a larger value of the radiative heat flux as estimated with the new model, but it still displays the increasing trend towards the edges. This outcome may appear a quite poor result of the revision process but, before drawing any conclusion, it is worthwhile discussing about that.

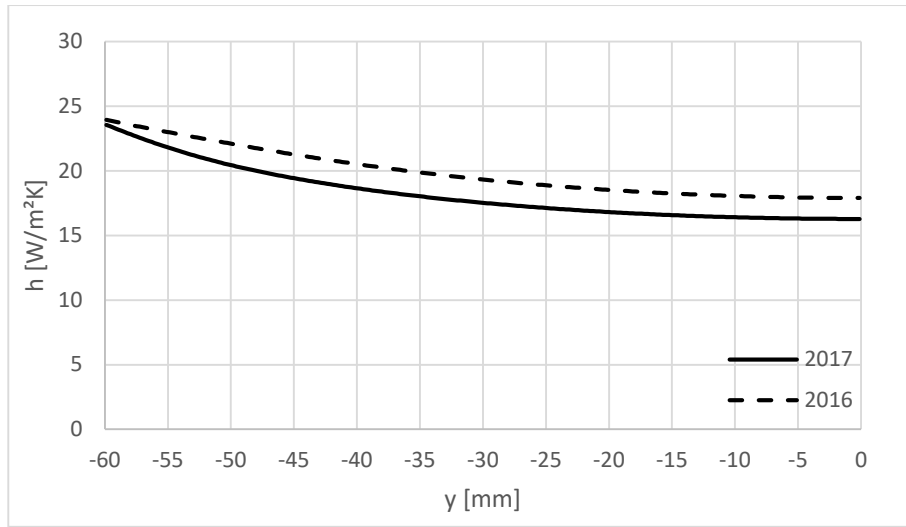


Figure 9. Ref. [1] (2016) vs present work (2017) local heat transfer estimate from the same experimental data, $Re=5400$

4.2 Numerical assessment of the model

An estimate of the overall error due to modeling issues can be carried out by comparing the local heat transfer coefficient based on q_c' from equation 17, to the ones evaluated by using for q_{kz} and q_{kxy} the values calculated by means of the numerical 2D FEM model; more precisely, we define

$$err = \frac{q_c'}{q_c} - 1 \equiv \frac{h'}{h} - 1 \quad (18)$$

It is important to notice that this estimated error is based solely on the numerical model, therefore eventual experimental issues are not taken into account. As it can be seen in figure 10, errors lie beneath 4% up to 40 mm from the centerline, and tend to diverge towards the edges. An increase of the Reynolds number reduces local errors, while the trend is unchanged. Figure 11 shows in detail the extent of the region where error is equal to or larger than 5% as a function of Reynolds numbers. As it can be see this region extends from the wall sides for a length ranging from 8 to 12 mm while Reynolds spacing from 8000 to 700.

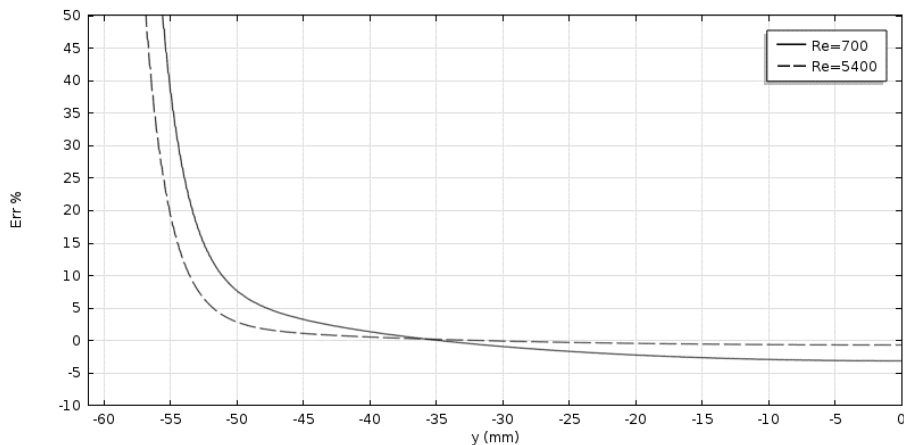


Figure 10. Error maps of h , for $Re=700$ and for $Re=5400$

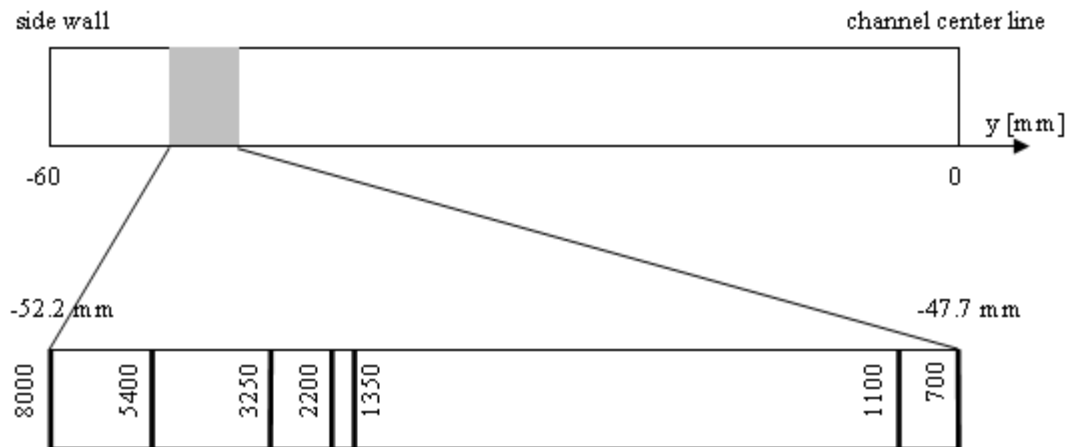


Figure 11. Spanwise positions of 5% error, as function of Reynolds number

Finally, a new estimate of the local convective coefficient can be made by correcting the approximation h' with the calculated error, as in the following:

$$h'_{\text{mod}} = \frac{h'}{\text{err} - 1} \quad (19)$$

The results are shown in figure 12 and are much closer to the expected values. In particular, h'_{mod} shows a flatter behavior in the central zone while tending to zero towards the edges. The conductive contribution near the edges has been proved to be the main source of error while estimating the spanwise distribution of h . Further issues could be linked to other aspects, which are already taken into account to our best knowledge but that could be more deeply investigated, like the influence of directional radiative properties on the radiative heat flux.

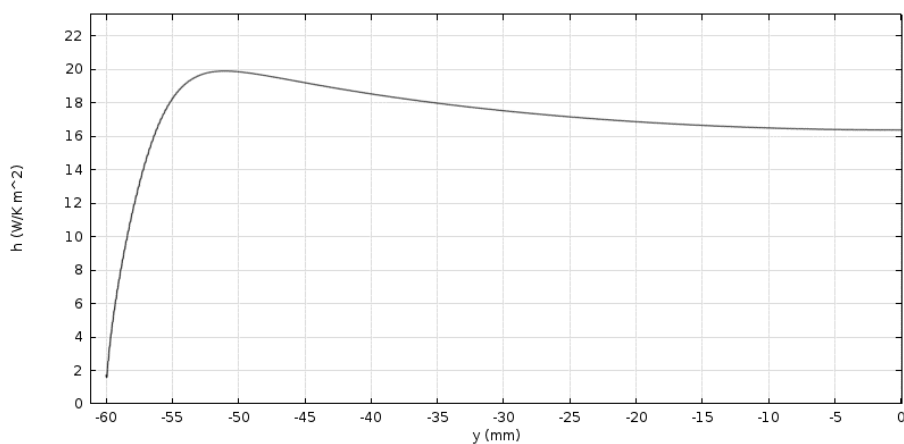


Figure 12. Estimate of local heat corrected by equation 19, Re=5400

5 Conclusions

This work consisted in a critical assessment of the processing techniques adopted to retrieve from experimental thermographic measurements the distribution of local convective heat flux, and therefore

of local convective heat transfer coefficient, in a forced air flow through a rectangular channel. The radiative model has been improved, and now it takes into account semi-transparent surface, with spectral-dependant properties. The contribution of the conductive terms, both inside PCB and towards its backside, has been deeply evaluated with the aid of numerical FEM models. The results show that the models based only on the surface and backside temperatures can approximate well the pseudo-conductive heat flux in the central part, but fail while moving towards the edges. Then, the estimate of the error has been used to provide a better evaluation of the convective heat transfer coefficient, which is actually closer to the expected behaviour in the non-ribbed channel. This kind of correction will be applied to ribbed geometry, while future work by means of DNS simulations will also provide a further support for the results.

References

- [1] D Fustinoni, P Gramazio, L Vitali and A Niro 2017 *J. of Phys.: Conf. Series* **796** 012015
- [2] D Fustinoni, P Gramazio, L P M Colombo and A Niro 2012 *J. Phys.: Conf. Ser.* **395** 012042
- [3] S Kakaç, R K Shah, W Aung, Handbook of single-phase convective heat transfer, Wiley-Interscience, 1987
- [4] M F Modest, Thermal radiation heat transfer, Elsevier Inc, 2013
- [5] R Siegel 1973 Net Radiation Method for Enclosure Systems Involving Partially Transparent Walls, NASA technical note D-7384